J. Fluid Mech. (1993), *vol.* 251, *pp.* 149–172

The influence of swirl and confinement on the stability of counterflowing streams

By J. D. GODDARD, A. K. DIDWANIA AND C.-Y. WU

Department of Applied Mechanics and Engineering Sciences, University of California, San Diego, La Jolla CA 92093-0310, USA

(Received 10 July 1992 and in revised form 5 December 1992)

A linear stability analysis of laterally confined swirling flow is given, of the type described by Long's equation in the inviscid limit or by the von Kármán similarity equations in the absence of lateral confinement. The flow of interest involves identical counterflowing fluid streams injected with equal velocity W_0 through opposing porous disks, rotating with angular velocities Ω and $\pm\Omega$, respectively, about a common normal axis. By means of mass transfer experiments on an aqueous system of this type we have detected an apparent hydrodynamic instability having the appearance of an inviscid supercritical bifurcation at a certain $|\Omega| > 0$. As an attempt to elucidate this phenomenon, linear stability analyses are performed on several idealized flows, by means of a numerical Galerkin technique. An analysis of high-Reynolds-number similarity flow predicts oscillatory instability for all non-zero Ω. The spatial structure of the most unstable modes suggests that finite container geometry, as represented by the confining cylindrical sidewalls, may have a strong influence on flow stability. This is borne out by an inviscid stability analysis of a confined flow described by Long's equation. This analysis suggests a novel bifurcation of the inviscid variety, which serves qualitatively to explain the results of our mass transfer experiments.

1. Introduction

The present work stems in part from the design of a laboratory device capable of generating a uniformly accessible surface for convective heat or mass transport between fluid streams. In previous works on the subject (Goddard, Melville & Zhang 1987; Zhang & Goddard 1989) it has been shown, by yet another variant of the Kármán similarity equation, that the requisite flow field can in principle be realized by means of counterflowing rotating fluid streams, such as might be created by uniform injection through porous rotating disks. A similar flow configuration has also been the subject of recent theoretical and experimental investigations of the effects of swirl on gaseous flames (Kim, Libby & Williams 1992).

For the purposes of the present discussion and for later reference, we recall that for steady similarity flows of the von Kármán type, the surface-normal velocity depends spatially only on surface-normal distance z with, say, $v_z = W(z)$. Hence, the mass (or heat) transfer coefficient at a planar stagnation surface $z = 0$ between counterflowing rotating streams is given asymptotically for large Péclet numbers by the non-dimensional surface-normal velocity gradient $W'(0)$ as (Zhang & Goddard 1989)

$$Nu = \left[-\frac{2W'(0)}{\pi}\right]^{\frac{1}{3}} Pe^{\frac{1}{3}} \quad \text{for} \quad W'(0) < 0, \tag{1}$$

where Nu and Pe denote the appropriate Nusselt and Péclet numbers and the primes

denotes derivatives with respect to z. In general, $W'(0)$ depends parametrically on the property ratios of the fluid streams, and on a characteristic Reynolds number Re and rotation parameter or inverse Rossby number Ro:

$$Re = W_0 d/\nu \quad \text{and} \quad \kappa = \Omega d/W_0 = Ro^{-1}, \tag{2}$$

where Ω, d and W_0 are disk rotation speed, disk separation and characteristic injection velocity, respectively. At large Re, the flow assumes an inviscid character, and $W'(0)$ becomes independent of Re.

A calculation of $W'(0)$ is given by Zhang & Goddard (1989) for property ratios characteristic of water and kerosene. As discussed in that work, the (Boussinesq) form (1) is valid only in the injection-dominated regime $\kappa < \pi$. At $\kappa = \pi$, where $W'(0) = 0$, it must be replaced by the (Lévêque) form

$$Nu = \frac{1}{\Gamma(\frac{4}{3})}[-\tfrac{1}{6}W''(0)]\, Pe^{\frac{1}{3}}, \tag{3}$$

which is characteristic of solid–fluid interfaces. The latter form reflects the fact that at the critical Rossby number $Ro = \pi^{-1}$ one attains a hydrodynamically 'frozen' fluid–fluid interface where surface stretching is annulled by the effects of rotation. At this point, viscous layers of characteristic thickness $O(Re^{-\frac{1}{3}})$ replace $O(Re^{-\frac{1}{2}})$ layers, and one enters the rotation-dominated regime $\kappa > \pi$ of inviscid cellular structures separated by multiple viscous interlayers (Zhang & Goddard 1989).

As is evident from the above discussion, rotation provides an additional degree of parametric freedom over and above simple stagnation flow, which may confer special advantages for the study of mass and heat transfer. Among these is the possibility of achieving a hydrodynamically frozen interface for processes such as the gas-phase deposition of fragile solid films onto smooth liquid substrates. The above considerations serve as a primary motivation for the present work, which is aimed at elucidating theoretically an apparent hydrodynamic instability revealed by the mass transfer experiments to be discussed below.

Hydrodynamic instability in this particular flow should come as no surprise, given the non-uniqueness of rotating-disk flows (Parter & Rajagopal 1984; Zandbergen & Dijkstra 1987; Goddard *et al.* 1987; Goldshtik & Javorsky 1989; Zhang & Goddard 1989) and the well-known instabilities of Ekman–von Kármán boundary layers (Greenspan 1968). Indeed, the stability of flow near rotating disks has been the subject of numerous theoretical investigations over the years, beginning with the works of Stuart and coworkers (Gregory, Stuart & Walker 1955) and including recent works by Szeri, Giron & Schneider (1983), Bodonyi & Ng (1983), Malik (1986) and Faller (1991), to name but a few. These studies, most of which rely on the type of local stability analysis pioneered by Gregory *et al.* (1955), confirm the magnitudes of critical Reynolds numbers observed in various experiments. However, in the rotating disk flow of interest here, one can anticipate major differences, in that strong injection of fluid at the bounding disks will blow all viscous layers off the disks and onto a weak Prandtl layer at the central stagnation surface (Zhang & Goddard 1989). To terms of lowest order in Re, one would expect this layer to have a negligible effect on the globally inviscid base flow and its stability.

As background for the subsequent theoretical stability analysis, §2 describes our mass transfer experiments on counterflowing aqueous streams. As will be seen, the experimental data are consistent with the inviscid limit of (1) for κ below a certain value, approximately 2.1, which, at first, we thought might represent a supercritical 'pitchfork' bifurcation. However, a subsequent linear stability analysis, presented here

in §4.1, indicates that the inviscid similarity flow is inviscidly unstable for all $\kappa > 0$. Moreover, we shall show that the addition of weak viscous effects do not serve to explain the observed stability of the flow for $\kappa \leqslant 2.0$. Although not in accord with experiment, this stability analysis of similarity flows provides an essential clue to the effects of finite container geometry, as represented by cylindrical sidewalls, on the stability of the base flow.

In §3, we make use of Long's equation (Fraenkel 1953; Batchelor 1967; Yih 1980) to compute the inviscid base flow, and in §4.2 we carry out an analysis of the linear stability of that flow to general three-dimensional disturbances, which suggests an uncommon type of bifurcation at $\kappa = 0$.

2. Mass-transfer experiments

We describe here the experimental apparatus and the electrochemical technique employed to study mass transfer between counterflowing aqueous streams, and we present the results of our mass transfer experiments. Those interested mainly in the subsequent stability analysis may proceed directly to §4.

2.1. *Experimental apparatus*

The apparatus is shown schematically in the definition sketch of figure 1. It consists of two rotatable plenum chambers covered by 8.8 cm diameter porous disks (D). The gap between the disks is fixed at $d = 2$ cm. Fluid is supplied by separate centrifugal pumps (P) to the chambers through hollow concentric shafts, each supported on duplex bearings and is driven at constant rotational speed by belt and pulley connected to an electronic tachometer, with provision for corotation or counter-rotation of the disks. The opposing fluid streams, injected through the porous disks with presumably uniform velocity, impinge at the fluid–fluid interface (I) positioned at the aperture of a splitter plate (S). The latter is situated at the midplane of the gap. Since the injectional Reynolds number Re is of the order of 10^3, the boundary layers on the splitter plate are assumed to have negligible influence on the flow over the aperture, at least for the base flow.

The flow cell is vibrationally isolated from pumps and motors by flexible rubberized tubing and drive belts. The circulation system for each cell consists of the centrifugal pump (P), a valve, air coolers (C), rotameters (F) and flexible tubing. Injection velocities, controlled by the valves, are monitored by rotameters (F). Flow rates of a few hundred cm^3/s and, hence, linear velocities of several tens of cm/s can be achieved in this set-up, corresponding to injectional Reynolds numbers of several thousand. Virtually arbitrary Rossby numbers Ro can be obtained by adjusting the rotational speeds. The fluid is maintained at constant temperature by the air coolers (C). The porous plates were made from 100 μm rigid stainless-steel screen, spot-welded onto stainless retainer plates.

In order to measure mass transfer between the counterflowing streams, an electrochemical technique was employed. Two sections of nickel pipes (E) serve as counter electrodes for electrochemical injection and removal of the electroactive species, which is thereby transferred steadily between upper and lower compartments under a steady applied voltage, controlled by a potentiostat. The resulting electrochemical current is measured by means of a digital multimeter, which by the Faraday equivalence gives the mass flux.

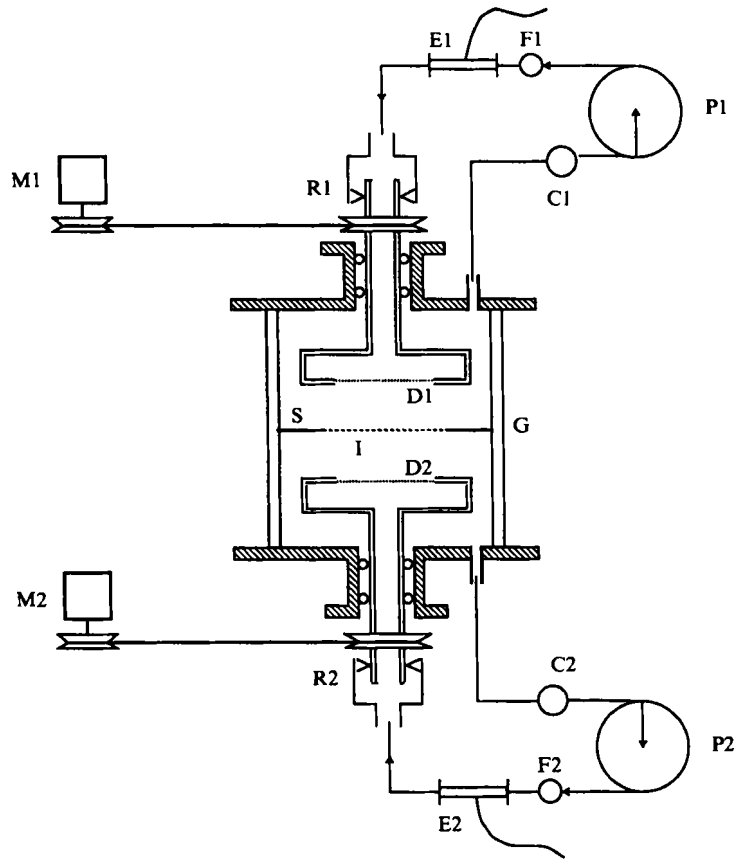

FIGURE 1. Schematic of flow facility (not to scale): C, air coolers; D, porous metal disks; E, nickel-tube electrodes; F, flow (rota) meters; G, glass wall; I, liquid–liquid interface; M, variable-speed DC motors, with digital tachometers; P, centrifugal pumps; R, rotating seals; S, splitter plate.

2.2. *Experimental procedures*

The well-known potassium ferricyanide/ferrocyanide (in aqueous KOH) redox reactions (Gordon, Newman & Tobias 1966) was employed as the electrochemical system:

$$\text{cathode:} \quad Fe(CN)_6^{-3} + e^- \rightarrow Fe(CN)_6^{-4},$$

$$\text{anode:} \quad Fe(CN)_6^{-4} \rightarrow Fe(CN)_6^{-3} + e^-.$$

The ferricyanide concentrations in small samples withdrawn periodically from the upper and lower compartments were monitored by means of a UV-visible spectrophotometer in the wavelength range 340–480 nm. Ferrocyanide ion has no absorbance peaks, while ferricyanide absorbs strongly around $\lambda = 424$ nm. Temperature had to be carefully controlled during spectrophotometric measurements, since the optical absorbance is affected by temperature. The details of the measurements are described by Wu (1991).

Experiments were carried out in solutions with molar concentrations

$$C_{KOH} = 5.9 \times 10^{-4} N, \quad C_{Ferro} = 5 \times 10^{-3} N, \quad C_{Ferri} = 4.85 \times 10^{-3} N.$$

The density, viscosity and diffusion coefficients at different temperature were calculated by an empirical formula given by Gordon *et al.* (1966). In order to assure that

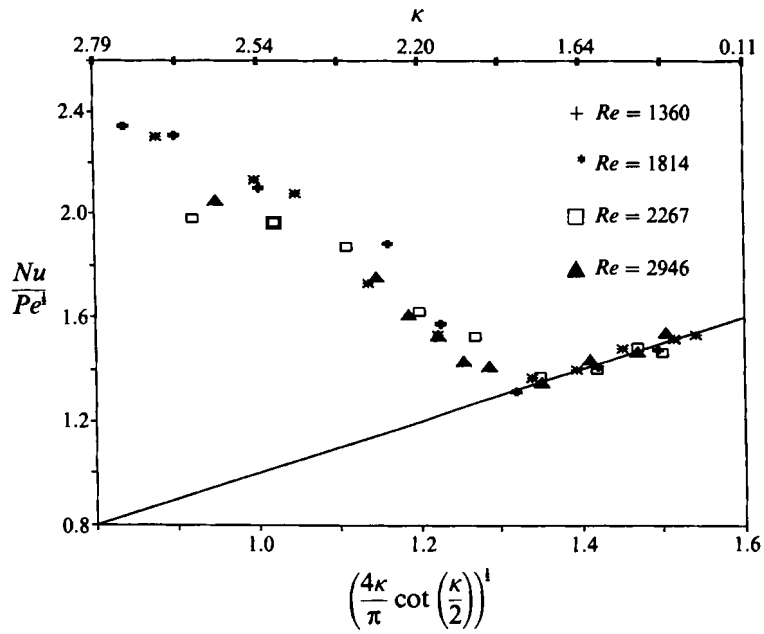

FIGURE 2. Experimentally determined interfacial mass transfer, for corotational flows at different Reynolds number. Solid line is theory for $\kappa < \pi$.

potassium ferrocyanide/ferricyanide is the only redox reaction occurring at the counter electrodes, so that electrochemical current reflects the actual mass transfer rate (without e.g. electrolysis of water), the DC voltage level was maintained below 0.6 V. To achieve accurately detectable concentration differences ΔC of ferricyanide ion, at these voltage levels and with the relatively high mass transfer coefficients in this system, it was necessary to restrict the mass transfer area. This was achieved by installation of a splitter plate with a small, 2 cm diameter, central aperture.

Measurements of concentrations and electrochemical currents were taken at different voltage levels. The slope of the remaining linear plot of ΔC versus I_0 at various Reynolds and Rossby numbers yields the mass transfer coefficient. In order to investigate the hydrodynamic limitations on the operation of the flow cell, a rather large region of Re–κ parameter space was investigated. The Nusselt and Péclet numbers are of the order of 10^3 and 10^6, respectively. Hence, the magnitudes of $Nu/Pe^{\frac{1}{2}}$ are of order unity.

2.3. *Results and discussion*

Experiments were conducted with corotating disks at equal rotational speeds, and at four different injectional Reynolds number: 1360, 1814, 2267 and 2946. Various values of κ were achieved by increasing the rotational speed from rest. The values of κ were chosen to lie below π, so that the flow was always in the injection-dominated regime for similarity flows (Goddard *et al.* 1987). The experiments were repeated with counter-rotating disks, at equal speeds for Reynolds number 2267 and the same values of κ as before.

The results of the experiments are presented in figure 2 as plots of the experimentally derived values of $Nu/Pe^{\frac{1}{2}}$ versus theoretical values, given below in equation (39) for the simplest inviscid similarity flow.

From figure 3 it is seen that the mass transfer for counter-rotating flow is almost the

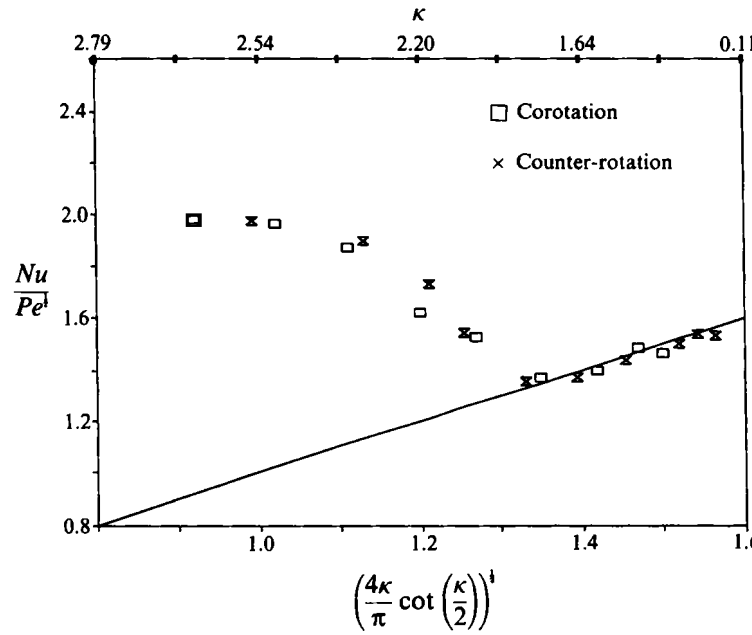

FIGURE 3. Experimentally determined interfacial mass transfer, for counter-rotational flows at injectional Reynolds number $Re = 2267$. Solid line is theory for $\kappa < \pi$.

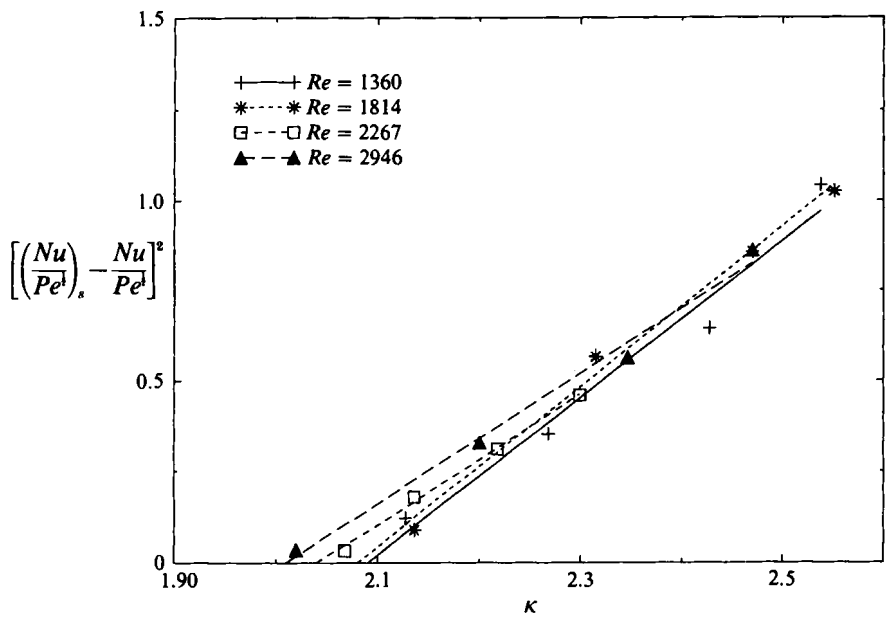

FIGURE 4. 'Supercritical' $[(Nu/Pe^{\frac{1}{2}})_s - Nu/Pe^{\frac{1}{2}}]^2$ as a function of inverse Rossby number at various Reynolds numbers.

same as that for corotating flow. The experimentally observed mass transfer is, therefore, in good agreement with theoretical predictions below certain values of κ, whereas an abrupt increase in mass transfer occurs above an ostensible critical value of κ which appears to lie in the range 2.01–2.09. Since such behaviour might reflect a

Re	κ_c	*a* (SD)	*b* (SD)
1360	2.09	2.17 (0.28)	−4.54 (0.65)
1814	2.08	2.24 (0.13)	−4.66 (0.31)
2267	2.04	1.82 (0.06)	−3.73 (0.13)
2946	2.01	1.8 (0.12)	−3.63 (0.28)

TABLE 1. Summary of parameter deduced from (5) from mass transfer data at various Reynolds numbers

subcritical bifurcation with hysteresis, all the experiments were repeated, for both counter-rotating and corotating disks and for the same values of Reynolds number and κ, by decreasing the rotational speed from an initial high level. No hysteresis was observed within the scatter of our experimental data.

Since the branching of the curve at $\kappa \approx 2.0$ appears similar to what one might expect from a supercritical bifurcation of the underlying convective flow, we were led to attempt a qualitative application of the Landau idea (Drazin & Reid 1989), according to which a disturbance amplitude A_e in a steady bifurcated state is given by

$$A_e \propto (\kappa - \kappa_c)^{\frac{1}{2}} \quad \text{as} \quad \kappa \downarrow \kappa_c. \tag{4}$$

Thus, above $\kappa \approx 2.0$ we attempt to correlate our data in the form:

$$\left[\left(\frac{Nu}{Pe^{\frac{1}{3}}}\right)_s - \frac{Nu}{Pe^{\frac{1}{3}}}\right]^2 = \left[\left(\frac{4\kappa}{\pi}\cot\frac{\kappa}{2}\right)^{\frac{1}{2}} - \frac{Nu}{Pe^{\frac{1}{3}}}\right]^2 = a\kappa + b \tag{5}$$

in which the left-hand side is taken to represent the disturbance amplitude A_e.

Figure 4 shows the resulting plot of $[(Nu/Pe^{\frac{1}{3}})_s - Nu/Pe^{\frac{1}{3}}]^2$ versus κ at various Reynolds numbers, which is indeed roughly linear. The intercept on the κ-axis gives the apparent critical values κ_c, listed in table 1, along with the standard deviations (SD) of *a* and *b*. While it is highly tempting to interpret the above results as an inviscid bifurcation from an inviscid base state at a definite $\kappa_c > 0$, the following stability analysis indicates otherwise.

3. Inviscid theory for the base flow

To account eventually for the effects of a finite container, the idealization shown in figure 5 is adopted as the flow geometry. There, two ring sinks, situated at the edge of porous rotating disks, remove fluid injected uniformly through the disks. The Euler and continuity equations governing the assumed steady axisymmetric base flows are

$$\frac{DU}{Dt} - \frac{V^2}{r} = -\frac{\partial}{\partial r}\left(\frac{P}{\rho}\right), \tag{6}$$

$$\frac{DV}{Dt} - \frac{UV}{r} = 0, \tag{7}$$

$$\frac{DW}{Dt} = -\frac{\partial}{\partial z}\left(\frac{P}{\rho}\right), \tag{8}$$

$$\frac{1}{r}\frac{\partial rU}{\partial r} + \frac{\partial W}{\partial z} = 0, \tag{9}$$

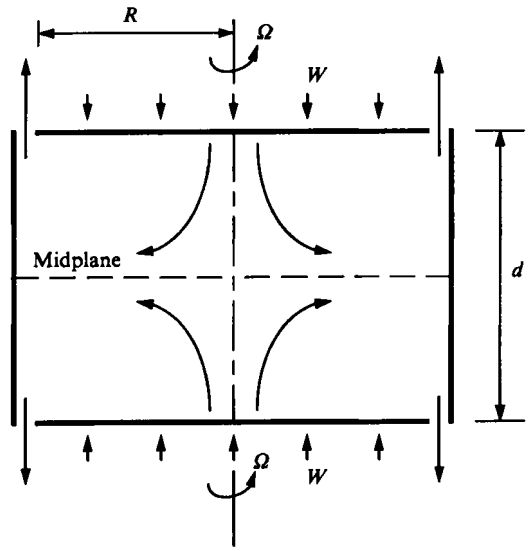

FIGURE 5. Idealized sketch of flow geometry.

where
$$\frac{\mathrm{D}}{\mathrm{D}t} = U\frac{\partial}{\partial r} + W\frac{\partial}{\partial z}, \tag{10}$$

with vertical boundary conditions, and at the disks

$$V = \Omega^{\pm} r, \quad \psi = \mp\tfrac{1}{2}W_0 r^2 \quad \text{at} \quad z = \pm\tfrac{1}{2}d \quad \text{for} \quad r < R, \tag{11}$$

where $\Omega^+ = \Omega^- = \Omega$ for corotation and $\Omega^+ = -\Omega^- = \Omega$ for counter-rotation, and ψ is the Stokes stream function defined by

$$U = -\frac{1}{r}\frac{\partial\psi}{\partial z}, \quad W = \frac{1}{r}\frac{\partial\psi}{\partial r}. \tag{12}$$

To represent the solid sidewalls, we further take

$$\psi = 0 \quad \text{at} \quad r = R. \tag{13}$$

In the standard way (Fraenkel 1953; Batchelor 1967; Yih 1980), (6)–(9) are then reduced to Long's equation:

$$\left(\frac{\partial^2}{\partial r^2} - \frac{1}{r}\frac{\partial}{\partial r} + \frac{\partial^2}{\partial z^2}\right)\psi + \tfrac{1}{2}f'(\psi) = r^2 h(\psi), \tag{14}$$

where $h(\psi)$ is usually determined from some 'upstream' flow condition, as

$$h(\psi) = \mathrm{d}\mathscr{H}(\psi)/\mathrm{d}\psi, \tag{15}$$

where $\mathscr{H}(\psi)$ is total head:

$$\mathscr{H}(\psi) = \tfrac{1}{2}(U^2 + V^2 + W^2) + p/\rho. \tag{16}$$

From the boundary conditions (11) it then follows that

$$f(\psi) = (4\Omega^2/W_0^2)\psi^2. \tag{17}$$

By introducing non-dimensional variables

$$\psi' = \frac{\psi}{W_0 R^2}, \quad r' = \frac{r}{R}, \quad z' = \frac{z}{d}, \quad h' = \frac{hd^2}{W_0}, \quad \alpha = \frac{d}{R}, \tag{18}$$

then dropping primes, we obtain from (14)–(17) the following non-dimensional equation:

$$\left(\frac{\partial^2}{\partial r^2}-\frac{1}{r}\frac{\partial}{\partial r}+\frac{1}{\alpha^2}\frac{\partial^2}{\partial z^2}\right)\psi+\frac{4\kappa^2}{\alpha^2}\psi=\frac{r^2h(\psi)}{\alpha^2}, \tag{19}$$

where α is the (inverse) aspect ratio.

We note that (19) and (11) imply that

$$\left(\frac{1}{2\psi}\frac{\partial^2\psi}{\partial z^2}\right)_{z=\pm\frac{1}{2}\alpha}=\mp h(\psi)-2\kappa^2=\Gamma(\psi). \tag{20}$$

In general the left-hand side of this equation may be an arbitrarily complicated function of r such that Γ and, hence, $h(\psi)$ are nonlinear functions of ψ. However, in at least two limiting cases of the present problem $\Gamma(\psi)$ becomes independent of ψ, implying a constant value of h.

In the first case, $\alpha\to\infty$ with a uniform flow W_0 and constant swirl Ω at infinity, $\Gamma(\psi)$ may be set equal to zero and $h(\psi)$ takes on one of the constant values $\mp 2\kappa^2$. Even relatively simple flows of this type exhibit very complex behaviour and have been widely investigated for a variety of situations (Greenspan 1968; Yih 1980).

The second case, $\alpha\to 0$, corresponds to infinite rotating disks where the flow is governed by the Kármán similarity form of the Euler equations, whose solutions, presented by Goddard *et al.* (1987), are cited below in §4. We obtain from these solutions a constant value of h independent of ψ:

$$h=\mp\frac{\kappa^2\cos\kappa}{\sin^2\frac{1}{2}\kappa}. \tag{21}$$

In general, for finite disks with finite spacing, there is no known simple expression for $h(\psi)$. In what follows, we merely assume that h is independent of ψ, which results in the standard linear form of Long's equation:

$$\left(\frac{\partial^2}{\partial r^2}-\frac{1}{r}\frac{\partial}{\partial r}+\frac{1}{\alpha^2}\frac{\partial^2}{\partial z^2}\right)\psi+\frac{4\kappa^2}{\alpha^2}\psi=-\frac{2q\kappa^2r^2}{\alpha^2}, \tag{22}$$

where q is a constant independent of ψ. For similarity flows $\alpha=0$ and (21) corresponds to

$$q_0=\pm\frac{\cos\kappa}{2\sin^2\frac{1}{2}\kappa}. \tag{23}$$

The general solution to (22) can be written down immediately as (Fraenkel 1953; Yih 1980)

$$\psi=-\frac{qr^2}{2}+MrJ_1\left(\frac{2\kappa r}{\alpha}\right)-r\sum A_n[\cos\gamma_n(z-\tfrac{1}{2})+C_n\sin\gamma_n(z-\tfrac{1}{2})]J_1(\lambda_n r)+(Sr^2+T)(\cos 2\kappa z+B\sin 2\kappa z), \tag{24}$$

where λ_n are roots of the Bessel function $J_1(\lambda)$, $\gamma_n=(4\kappa^2-\lambda_n^2\alpha^2)^{\frac{1}{2}}$ and M, A_n, C_n, S, T, B are constants to be determined from the appropriate boundary conditions. We note the alternative representation for ψ:

$$\psi=-\frac{qr^2}{2}+MrJ_1\left(\frac{2\kappa r}{\alpha}\right)-r\sum A_n[\cos\tau_n(z-\tfrac{1}{2})+C_n\sin\tau_n(z-\tfrac{1}{2})]J_1\left(\frac{\nu_n r}{\alpha}\right)+(Sr^2+T)(\cos 2\kappa z+B\sin 2\kappa z), \tag{25}$$

where τ_n are certain roots of trigonometric functions, $\nu_n = (4\kappa^2 - \tau_n^2\alpha^2)^{\frac{1}{2}}$ and the constants M, A_n, C_n, S, T, B are generally distinct from those in (24). The representation (24) involves radial eigenmodes whereas the second, (25), involves vertical modes. We choose the representation (24) for our subsequent analysis, since it approaches in an obvious manner the similarity solution in the limit $\alpha \to 0$.

For flow between finite disks with finite spacing, the expression for $h(\psi)$ given by (15)–(16) reduces at $z = \pm\frac{1}{2}$ to,

$$h = \frac{\mathrm{d}\mathscr{H}(\psi)}{\mathrm{d}\psi} = \frac{\mathrm{d}(U^2+2p)}{\mathrm{d}r^2} + \kappa^2. \tag{26}$$

Since the radial pressure gradient is generally not constant, this implies that, if h is to be constant, we must relax the condition of no slip $U = 0$ at the disks, which in any event arises somewhat fortuitously in the inviscid limit for the above similarity flow. However, as will be seen from the numerical computations below, the no-slip condition still holds approximately over much of the central portion of the porous disks, breaking down only in the sink-dominated regions near their edges. While this appears to have negligible consequences for the inviscid limit of interest here, it does suggest that any attempt to account for higher-order viscous effects would require strong boundary layers on the disks near their periphery.

For the inviscid limit of interest, we adopt the boundary conditions

$$\psi = 0 \quad \text{at} \quad r = 0 \quad \text{for} \quad |z| \leqslant \tfrac{1}{2}, \tag{27}$$

$$\psi = 0 \quad \text{at} \quad z = 0 \quad \text{for} \quad 0 \leqslant r < 1, \tag{28}$$

$$\psi = \mp\tfrac{1}{2}r^2 \quad \text{at} \quad z = \pm\tfrac{1}{2} \quad \text{for} \quad 0 \leqslant r < 1. \tag{29}$$

Then (29) and (28) yield

$$A_n = \frac{1 - q4\kappa^2/\gamma_n^2}{\lambda_n J_0(\lambda_n)}, \tag{30}$$

$$C_n = (4q\kappa^2/\gamma_n^2)\operatorname{cosec}(\tfrac{1}{2}\gamma_n) - \cot(\tfrac{1}{2}\gamma_n), \tag{31}$$

for $n = 1, 2, \ldots$, together with $S = 0$, $T = 0$, and

$$M = \frac{q}{2J_1(2\kappa/\alpha)}. \tag{32}$$

The base-flow velocity components are given then by

$$U = \Sigma A_n \gamma_n [-\sin\gamma_n(z-\tfrac{1}{2}) + C_n \cos\gamma_n(z-\tfrac{1}{2})] J_1(\lambda_n r), \tag{33}$$

$$V = \frac{2\kappa}{\alpha}\left\{\frac{qrJ_1(2\kappa r/\alpha)}{2J_1(2\kappa/\alpha)} - \frac{qr^2}{2} + \Sigma A_n[\cos\gamma_n(z-\tfrac{1}{2}) + C_n \sin\gamma_n(z-\tfrac{1}{2})] J_1(\lambda_n r)\right\}, \tag{34}$$

$$W = -q + \frac{\kappa}{\alpha}\frac{qrJ_1(2\kappa r/\alpha)}{J_1(2\kappa/\alpha)} + \Sigma A_n \lambda_n [\cos\gamma_n(z-\tfrac{1}{2}) + C_n \sin\gamma_n(z-\tfrac{1}{2})] J_0(\lambda_n r). \tag{35}$$

The constant q remains to be specified and, as we noted earlier, we have no *a priori* value for it except in the limiting cases $\alpha = 0$ and $\alpha \to \infty$. In what follows, we treat q as a free parameter and examine the influence on the base flow and its stability. In particular, we will choose the limiting value of q_0 for similarity flow as a reference point and examine the sensitivity of the results to variations about q_0. We now present our computations of the base flow and the mass transfer coefficients and compare them with the limiting case of similarity flow $\alpha \to 0$.

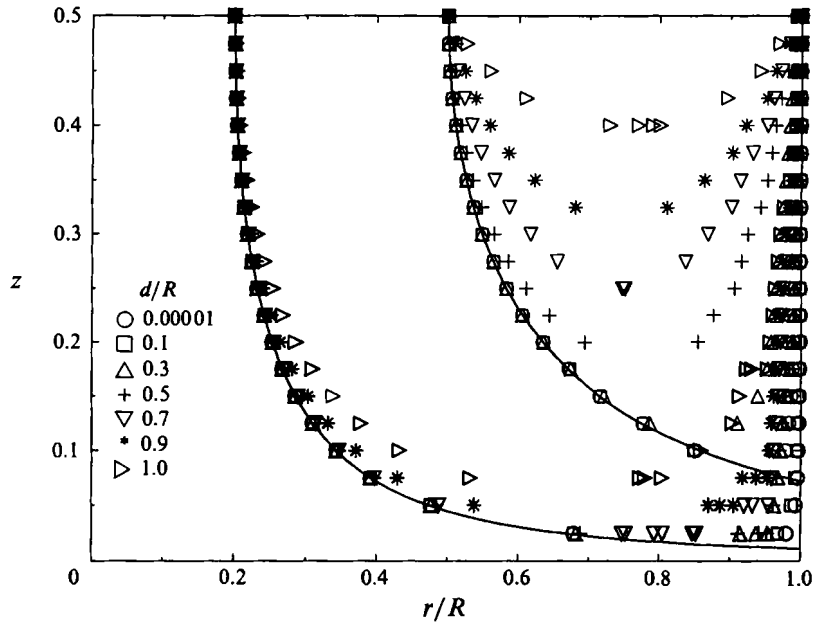

FIGURE 6. Streamlines in meridional plane for various values of d/R. Solid lines represents the similarity solution.

In figure 6 we present streamlines for different α values. As the aspect ratio α^{-1} becomes large, the stream surfaces obtained from Long's equation obviously approach the similarity form. We find that with increasing κ the flow is swept radially outwards much faster and departures from similarity are stronger. We also note that for κ small, the streamlines are almost unaffected by q, whereas at higher values of κ the effects are much more pronounced.

The expression for the local interfacial mass transfer coefficient in the injection-dominated region is given asymptotically for large Pe by the non-dimensional form

$$Nu(r) = c_1(r)\, Pe^{\frac{1}{2}}, \tag{36}$$

where $c_1(r)$ is given by

$$c_1(r) = \frac{\psi_1(r)}{\pi^{\frac{1}{2}}\left[\int_0^r \psi_1(r)\, r\, \mathrm{d}r\right]^{\frac{1}{2}}} \tag{37}$$

(Acrivos & Goddard 1966) with

$$\psi_1(r) = -(\mathrm{d}\psi/\mathrm{d}z)_{z=0} = rU(r,z)|_{z=0}, \tag{38}$$

where U is given by (33). In the limit $\alpha \to 0$, we have $\psi = \frac{1}{2}[r^2 W(z)]$ and, for the inviscid flow at hand, this gives the similarity form

$$\frac{Nu}{Pe^{\frac{1}{2}}} = \left(\frac{Nu}{Pe^{\frac{1}{2}}}\right)_s = \left(\frac{4\kappa}{\pi}\cot\frac{\kappa}{2}\right)^{\frac{1}{2}}, \tag{39}$$

which follows from (57)–(60). In figure 7, we show the effect of variation in values of α on the ratio of mass transfer coefficients $Nu(r)/Nu_s$ computed from (35). As indicated in this figure, the mass transfer remains practically uniform in the central region of the midplane, over which our experimental transfer coefficients were actually measured. It is also observed that mass transfer is very weakly affected by changes in the values of

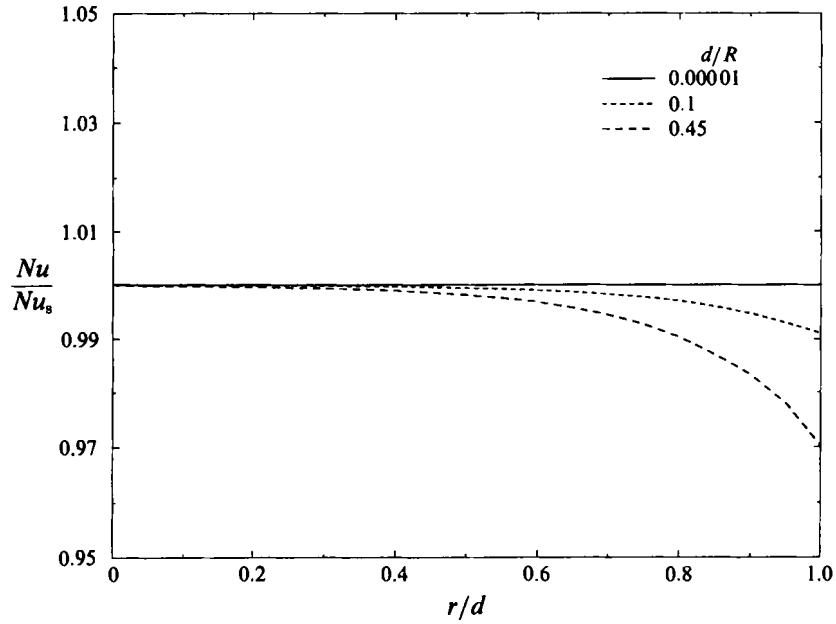

FIGURE 7. $Nu(r)/Nu_s$ as a function of r/d for various α.

q (a 50% change in q changing the coefficient by only about 5%) and the latter change is nearly uniform over the central region. We now examine the linear stability of the above base flow.

4. Linear stability analysis

First we derive the equations governing three-dimensional perturbations, specify the associated boundary conditions and then describe the method of solution to obtain growth rates. Next, we consider the similarity limit $\alpha \to 0$ and, finally, we discuss linear stability for $\alpha > 0$.

We recall that, in terms of cylindrical coordinates (r, θ, z) and the corresponding perturbation velocity components (u, u, w) natural to our geometry, a general three-dimensional perturbation

$$\phi(r,\theta,z,t) = [u(r,\theta,z,t), v(r,\theta,z,t), w(r,\theta,z,t), p(r,\theta,z,t)] \tag{40}$$

on an axisymmetric steady base flow $[U(r,z), V(r,z), W(r,z), P(r,z)]$ satisfies the linearized non-dimensional equations,

$$\frac{\partial u}{\partial r}+\frac{u}{r}+\frac{1}{r}\frac{\partial v}{\partial \theta}+\frac{\partial w}{\partial z}=0, \tag{41}$$

$$\frac{\mathrm{D}u}{\mathrm{D}t}+u\frac{\partial U}{\partial r}+\frac{2Vv}{r}+w\frac{\partial U}{\partial z}=-\frac{\partial p}{\partial r}+\frac{1}{Re}\left[\frac{\partial}{\partial r}\left(\frac{1}{r}\frac{\partial (ru)}{\partial r}\right)+\frac{1}{r^2}\frac{\partial^2 u}{\partial \theta^2}+\frac{2}{r^2}\frac{\partial v}{\partial \theta}+\frac{\partial^2 u}{\partial z^2}\right], \tag{42}$$

$$\frac{\mathrm{D}v}{\mathrm{D}t}+u\frac{\partial V}{\partial r}+\frac{Uv}{r}+\frac{Vu}{r}+w\frac{\partial V}{\partial z}=-\frac{1}{r}\frac{\partial p}{\partial \theta}+\frac{1}{Re}\left[\frac{\partial}{\partial r}\left(\frac{1}{r}\frac{\partial (rv)}{\partial r}\right)+\frac{1}{r^2}\frac{\partial^2 v}{\partial \theta^2}+\frac{2}{r^2}\frac{\partial u}{\partial \theta}+\frac{\partial^2 v}{\partial z^2}\right], \tag{43}$$

$$\frac{\mathrm{D}w}{\mathrm{D}t}+w\frac{\partial W}{\partial z}=-\frac{\partial p}{\partial z}+\frac{1}{Re}\left[\frac{1}{r}\frac{\partial}{\partial r}\left(r\frac{\partial w}{\partial r}\right)+\frac{1}{r^2}\frac{\partial^2 w}{\partial \theta^2}+\frac{\partial^2 w}{\partial z^2}\right], \tag{44}$$

where
$$\frac{\mathrm{D}}{\mathrm{D}t} = \frac{\partial}{\partial t} + U\frac{\partial}{\partial r} + \frac{V}{r}\frac{\partial}{\partial \theta} + W\frac{\partial}{\partial z}, \tag{45}$$

and where in addition to the variables (18) the non-dimensional time

$$t' = W_0 t/d \tag{46}$$

is implied. Although we shall mainly focus on the limit $Re \to \infty$, we retain terms in Re^{-1}, in order to analyse weak viscous effects in the case of similarity flows.

Assuming that the perturbation $\phi(r, \theta, z, t)$ is regular at $r = 0$, we adopt a normal-mode representation

$$\phi(r, \theta, z, t) = \hat{\phi}(r, z)\, \mathrm{e}^{\mathrm{i}n\theta + \sigma t}, \tag{47}$$

where $n = 0, 1, 2, \ldots$, is the azimuthal wavenumber and σ the complex growth rate. This results in an eigenvalue problem for $\hat{\phi}(r, z) = \hat{\phi}_n(r, z)$ over the (r, z)-domain, with eigenvalues $\sigma(n, \kappa, \alpha, Re)$.

We treat the above problem numerically, by means of a Galerkin method (Fletcher 1984), with basis functions of the separable form $R_\lambda(r) Z_m(z)$ and subsequent representations for $\hat{\phi}$ of the form

$$\hat{\phi}(r, z) = \sum_\lambda \sum_m \hat{\phi}_{\lambda, m} R_\lambda(r) Z_m(z), \tag{48}$$

where λ and m are chosen from appropriate discrete or continuous sets. By means of (48), it is possible to represent various types of boundary conditions appropriate to the problem at hand, about which a few words are in order.

In the case of finite Re to be discussed below, we impose no-slip conditions in tangential components of velocity at the bounding surface $r = 1$, $z = \pm\frac{1}{2}$. However, in the inviscid limit such no-slip conditions are relaxed, except that the azimuthal perturbation v is still assumed to vanish at $z = \pm\frac{1}{2}$, in order to satisfy conservation of angular momentum of injected fluid.

On the other hand, all boundary-normal velocity perturbations are assumed always to vanish at $r = 1$, $z = \pm\frac{1}{2}$. For the latter boundaries, we note that the vanishing of normal velocity perturbations can be thought of as the limit, for $K \to 0$, of a more generally correct boundary condition connecting w and p:

$$w = \pm K(p - p_0) \quad \text{at} \quad z = \pm\tfrac{1}{2}, \tag{49}$$

where K is a hydraulic conductivity of the porous boundary A and p_0 is a 'supply pressure', which must be given by

$$p_0 = \frac{1}{A}\int_A p \, \mathrm{d}A \tag{50}$$

in order to maintain the overall volumetric injection of the base flow.†

Before carrying out the above expansions, it is convenient to eliminate the pressure, by cross-differentiation of the perturbation equations (42)–(44), and the vertical perturbation w, by means of the continuity equation (41). This reduces the problem to one of determining $[u, v]$.

For the vertical direction we then choose

$$Z_m(z) = \frac{1}{\sqrt{2}}\{[(-1)^m - 1]\cos m\pi z + [(-1)^m + 1]\sin m\pi z\} \tag{51}$$

† This more general boundary condition was suggested by an enlightening discussion with our colleague, Professor Paul Libby.

for $m = 1, 2, \ldots$, based on the fact that the inviscid base state itself is trigonometric. The trial functions $Z_m(z)$ vanish at the plates and form a complete orthonormal set on $(-\frac{1}{2}, \frac{1}{2})$. The choice of $R_\lambda(r)$ is governed by the lateral boundary conditions and will be made explicit below.

In the usual manner, the representation (48) is substituted into the equations and the residuals are required to be orthogonal to the chosen trial function, thus generating the linear system of equations for the expansion coefficients:

$$\boldsymbol{L}\boldsymbol{\phi} = \sigma \boldsymbol{M}\boldsymbol{\phi}. \tag{52}$$

Here $\boldsymbol{L}$ and $\boldsymbol{M}$ are complex non-Hermitian square matrices, whose order will ultimately be determined here by the number of (discrete) modes chosen in (48), and $\boldsymbol{\phi} = [\hat{\phi}_{\lambda, m}]$ is the unknown coefficient vector. The resulting eigenvalue problem

$$\det(\boldsymbol{L} - \sigma \boldsymbol{M}) = 0 \tag{53}$$

is solved to obtain σ as a function of the various parameters. The number of expansion modes in m and λ are varied in solving the eigenvalue problem until a convergence was achieved in the largest growth rate. We find that a modest number of modes, of the order of ten each in m and λ, gave convergence to at least three decimal places in the σ values. We discuss next the stability of flow between infinite disks.

4.1. *Large-Re similarity flows* ($\alpha = 0$)

For $\alpha = 0$ the base flow is described by the well-known Kármán–Bödewadt–Batchelor reduction of the Navier–Stokes equations (Zhang & Goddard 1989) which is equivalent to

$$Re^{-1} g''' + 2\,\mathrm{Re}(g)\, g'' - (g')^2 - C = 0, \tag{54}$$

where $()' = \mathrm{d}()/\mathrm{d}z$ and the cylindrical polar components of fluid velocity and the radial pressure gradient are given in terms of the complex dependent variable $g(z)$ as follows:

$$F + \mathrm{i}G = g'(z), \quad H = -2\,\mathrm{Re}(g) \tag{55}$$

and

$$\frac{1}{r}\frac{\partial P}{\partial r} = C, \tag{56}$$

where

$$[U, V, W] = [rF(z), rG(z), H(z)]. \tag{57}$$

The boundary conditions at the porous plates are

$$F = 0, \quad G = (\mp)\kappa, \quad H = \pm 1 \quad \text{at} \quad z = \mp\tfrac{1}{2} \tag{58}$$

with the signs for G being given in parentheses for the case of counter-rotating disks.

For large Reynolds number, in the injection-dominated region $\kappa < \pi$, the solution to the above equation can be expressed as

$$\begin{bmatrix} F \\ G \\ H \end{bmatrix} = \begin{bmatrix} F_0(z) + F_1(z)/Re + \ldots \\ G_0(z) + G_1(z)/Re + \ldots \\ H_0(z) + H_1(z)/Re + \ldots \end{bmatrix}. \tag{59}$$

The inviscid solution, which satisfies the no-slip boundary conditions at the porous disks, is given by

$$H_0 = \frac{\mathrm{sgn}(z)}{\cos^2(\frac{1}{2}\kappa) - 1}\left[\cos^2\kappa(z - \tfrac{1}{2}\,\mathrm{sgn}(z)) - \cos^2(\tfrac{1}{2}\kappa)\right], \tag{60}$$

$$G_0 = (\mp)\kappa H_0, \tag{61}$$

$$F_0 = -\frac{1}{2}\frac{\mathrm{d}H_0}{\mathrm{d}z}. \tag{62}$$

The viscous corrections $[F_1, G_1, H_1]$, given by Zhang & Goddard (1989) and amended here, are recorded in the Appendix.

The radial dependence of the base state suggests that general three-dimensional perturbations can be expressed as

$$\hat{\phi} = \sum_{\lambda} r^{\lambda} \phi_{\lambda}(z), \tag{63}$$

which is reminiscent of the planar case discussed by Brattkus & Davis (1990). Also, the neutral case $\sigma = 0$ corresponds to the 'spatial instability' of boundary layer flows discussed by Chen & Libby (1968). However, in general λ may be complex. Equation (63) corresponds of course to

$$R_{\lambda}(r) = r^{\lambda} \tag{64}$$

in (48), which formally represents a decomposition in terms of the Mellin transform (Erdélyi 1954) as opposed to the standard Fourier transform.

Writing
$$l = \mathrm{Re}(\lambda), \quad \beta = \mathrm{Im}(\lambda) \tag{65}$$

one sees that
$$r^{\lambda} e^{in\theta} = r^{l} e^{i(n\theta + \beta \log r)}, \tag{66}$$

whose phase represents the logarithmic spiral-form disturbance assumed in the local normal-mode analysis of Gregory *et al.* (1955). It arises quite naturally from the present treatment, which not only lends support to their representation but also provides a novel exact decomposition of general disturbances into spiral-form (Mellin) as opposed to plane-form (Fourier) modes. However, contrary to the analysis of Gregory *et al.* (1955), the former are generally not 'normal' modes, i.e. not uncoupled, as we next establish. While the spiral-form decomposition (66) has limited utility in the present problem it may prove useful for related stability analyses.

Assuming complete regularity of the modal amplitudes $|r^{\lambda}|$ at $r = 0$, we take l to be integral in (65) with $l = 1, 2, \ldots$, writing

$$\hat{\phi}_{\lambda}(z) = \hat{\phi}_{l}(z, \beta) = [u_l, v_l, w_l, p_l]. \tag{67}$$

Then, upon substituting this form of perturbation together with the base flow (55)–(56), into (41)–(44), we obtain the following eigenvalue problem in z, described by an infinite set of coupled ordinary differential equations:

$$(\lambda+1)u_l + inv_l + \mathrm{d}w_{l-1}/\mathrm{d}z = 0, \tag{68}$$

$$\begin{aligned}
&u_l[in\sigma + (\lambda+1)inF - Gn^2 - 2(\lambda+1)G] - v_l[(\lambda+1)\sigma + (\lambda+1)^2 F + inG(\lambda-3)] \\
&+ inH\frac{\mathrm{d}u_l}{\mathrm{d}z} - (\lambda+1)H\frac{\mathrm{d}v_l}{\mathrm{d}z} + w_l[inF' - (\lambda+1)G'] - Re^{-1}\left[in\frac{\mathrm{d}^2 u_l}{\mathrm{d}z^2} + (\lambda+1)\frac{\mathrm{d}^2 v_l}{\mathrm{d}z^2}\right] \\
&+ Re^{-1} v_{l+2}[(\lambda+1)[(\lambda+2)^2 - (n^2+1)] - 2n^2] \\
&+ Re^{-1} v_{l+2}[2in(\lambda+1) - in[(\lambda+2)^2 - (n^2+1)]] = 0,
\end{aligned} \tag{69}$$

$$\begin{aligned}
&\left[\sigma w_l + [(\lambda-1)F + inG + H']w_l + H\frac{\mathrm{d}w_l}{\mathrm{d}z} - Re^{-1}\left(\frac{\mathrm{d}^2 w_l}{\mathrm{d}z^2} + w_{l+2}\frac{[(\lambda+1)^2 - l^2]}{Re}\right)\right](\lambda-1) \\
&= \frac{\mathrm{d}}{\mathrm{d}z}\left\{\sigma u_{l-2} + [(\lambda+1)F + inG]u_{l-2} - 2Gv_{l-2} + H\frac{\mathrm{d}u_{l-2}}{\mathrm{d}z}\right. \\
&\qquad \left. + w_{l-2}F' - Re^{-1}\left[\frac{\mathrm{d}^2 u_{l-2}}{\mathrm{d}z^2} - [\lambda^2 - (n^2+1)]u_l + 2inv_{l+2}\right]\right\}
\end{aligned} \tag{70}$$

for $l = 1, 2, 3, \ldots$, with eigenvalues $\sigma = \sigma(n, l, \beta, \kappa, Re)$. Here, n, l, β relate to the

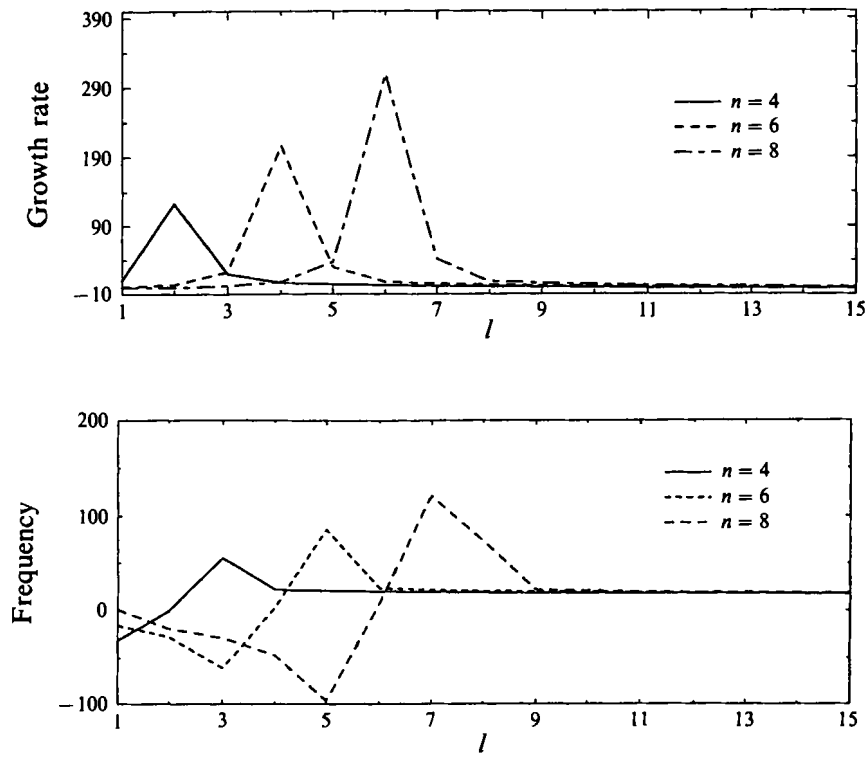

FIGURE 8. Growth rate and frequency *vs.* l for various values azimuthal wavenumbers n, at $\beta = 0.4$, $\kappa = 1.0$ and $Re = \infty$.

perturbation waveform while κ and Re characterize the base flow. The real part of σ represents the growth rate of the disturbance and the imaginary part its oscillation frequency. In line with the representation (48), we take

$$[u_l, v_l] = [u_{l,m}, v_{l,m}] Z_m(z) \tag{71}$$

for $l, m = 1, 2, 3, \ldots$, where the $Z_m(z)$ are given by (51). Thus the eigenvalue calculation (52) is tantamount here to a Fourier-trigonometric analysis of (69)–(70).

Using the solution method described earlier, we first examine the eigenvalues σ as functions of various parameters of interest for the inviscid base flow. Subsequently, we analyse the stability of a weakly viscous base state against viscous perturbations, by including the weakly viscous corrections indicated in (59) and retaining the term in Re^{-1} in (41)–(44).

4.1.1. *Results and discussion*

For a range of parameters (κ, Re) the maximum growth rate and the corresponding frequency as a function of n and l are computed. It is observed that axisymmetric disturbances ($n = 0$) are always stable, i.e. $\mathrm{Re}(\sigma) < 0$, for all values of κ. We note that Brady & Durlofsky (1987) have also predicted stability of similarity solutions against axisymmetric disturbances in the case of finite disks without injection. The computed growth rate and frequency for non-axisymmetric perturbations are shown in figure 8 as a function of l and n for $\kappa = 1.0$ and $\beta = 0.4$. The growth rate is zero at $\kappa = 0$ but is always positive for $\kappa > 0$, which is of course at odds with the ostensible critical values of about 2.1 observed in our experiments.

From figure 9, we see that weak viscous effects in the base flow and the perturbations

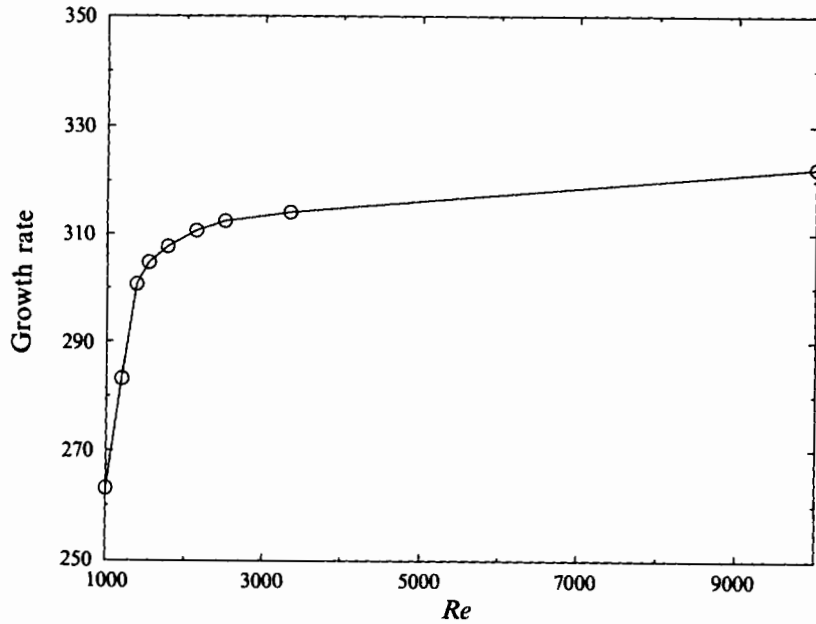

FIGURE 9. Growth rate *vs.* Reynolds number for $\kappa = 1.0$, $\beta = 0.1$, $n = 6$ and $l = 4$.

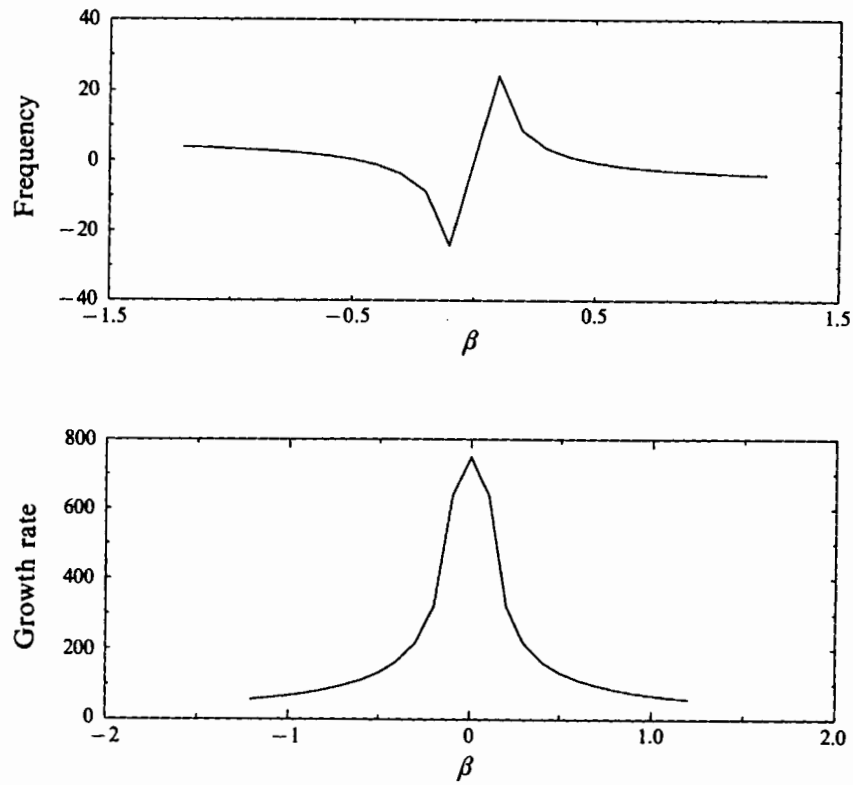

FIGURE 10. Growth rate and frequency *vs.* β for $\kappa = 1.0$, $n = 6$ and $l = 4$ and $Re = \infty$.

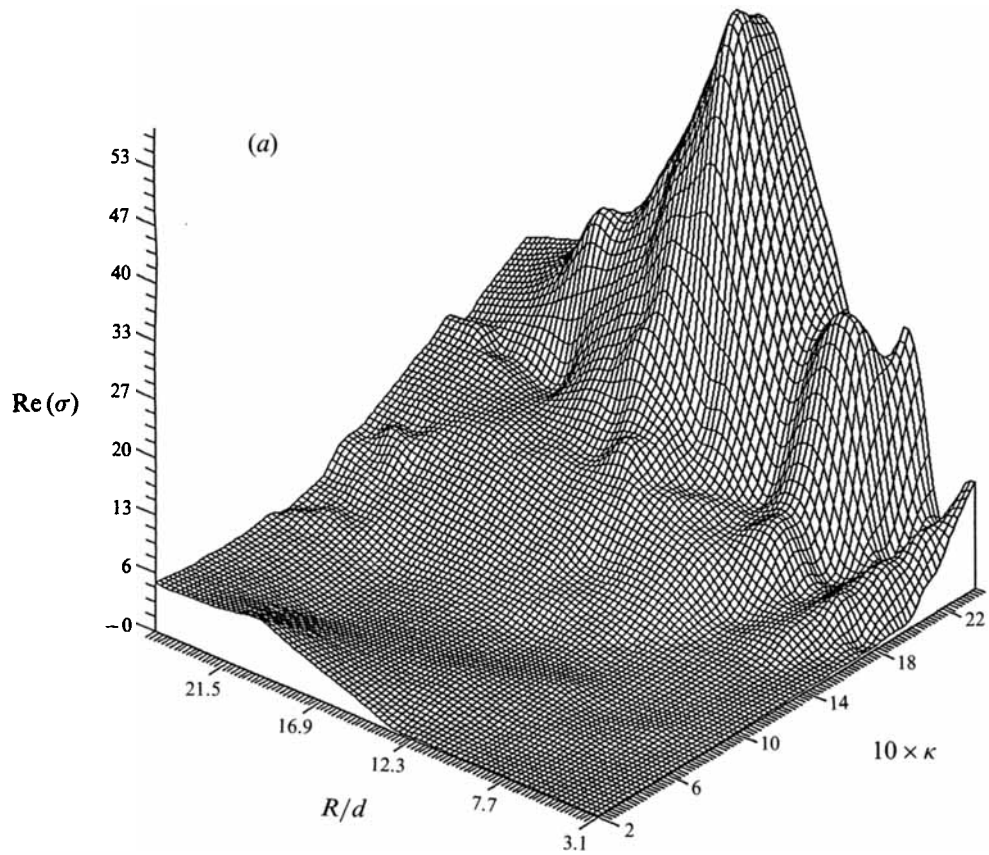

FIGURE 11(a). For caption see facing page.

reduce the growth rate but do not eliminate the instability, as the non-dimensional growth rates are still orders of magnitude larger than unity. In an attempt to represent possible stabilizing effects of the splitter plate at $z = 0$ we eliminated those modes (71) having even parity of $v_l(z)$, but this did not substantially affect growth rates.

In confined flows where the growth rates are not too large (as our computations in the next section indicate) one might expect the presence of viscosity to eliminate instability below some critical κ. Indeed, the visual observations, by Chen, Liu & Sohrab (1987), of radially finite gaseous flames in counterflowing swirling jets suggests that this critical κ-value may even exceed π. However, the stated agreement of their experimental results with inviscid theory (Sivashinsky & Sohrab 1987) is puzzling, in the light of the present stability considerations.

In figure 10, we see that for $\kappa = 1.0$, the growth rate exhibits a maximum at $\beta = 0$, which is also found to be the case for all other κ values. We find that the most unstable perturbations are characterized by $n = l+2$ and $\beta = 0$, where the coefficient matrix $\boldsymbol{M}$ in (52) becomes singular. Also, we find that these maximally unstable modes correspond to the special class of inviscid disturbances:

$$\phi = (r^{1+l}u_l(z), r^{1+l}v_l(z), r^{1+l}w_l(z), r^{2+l}p_l(z))\,\mathrm{e}^{\mathrm{i}n\theta+\sigma t} \tag{72}$$

which represent degenerate spirals, with vortical axis parallel to the r-direction and with an r-dependence resembling that of the base flow (57). The results are qualitatively the same for both corotating and counter-rotating disks.

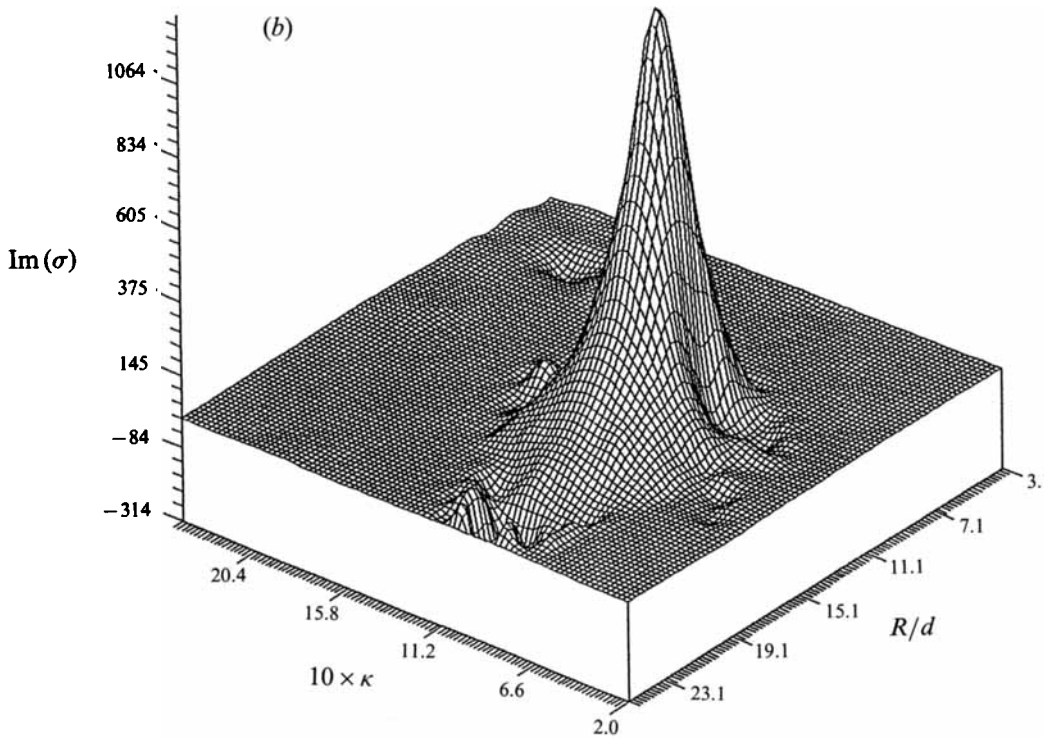

FIGURE 11. (*a*) Growth rate and (*b*) frequency as a function of aspect ratio and κ for corotating disks for azimuthal wavenumber $n = 2$.

The above results indicate that the axisymmetric similarity solutions are unconditionally unstable for all $\kappa > 0$, so that even a small amount of rotation destabilizes the simple inviscid stagnation flow. The occurrence of neutral stability for $\kappa = 0$ is somewhat reminiscent of the viscous stability of plane stagnation flow against disturbances of the form (72), with $n = 0$, $r \equiv x$, demonstrated by Brattkus & Davis (1990). In the present case, the growth rate (which we recall are scaled by d/W_0) become rapidly large as κ increases from $\kappa = 0$.

Since the largest growth rates occur for $\beta = 0$, this implies that the most unstable modes are not exactly Görtler-type instabilities, where one would expect to observe spiral modes with axes lying roughly along the base-flow streamlines. By contrast our unstable modes, with axes cutting across streamlines, appear to represent a combination of Görtler and inflexional-profile instabilities.

In attempting to explain the apparent discrepancy between theory and experiment, we note that the disturbance pressure associated with the most unstable modes (72) is harmonic in r and θ:

$$\frac{1}{r}\frac{\partial}{\partial r}\left(r\frac{\partial p}{\partial r}\right)+\frac{1}{r^2}\frac{\partial^2 p}{\partial \theta^2} = 0, \tag{73}$$

which provides a clue to the discrepancy. Since (elliptic) problems of the type (73) are highly sensitive to boundary conditions, one suspects that the effect of sidewalls on stability cannot be neglected, as we shall confirm in the next section.

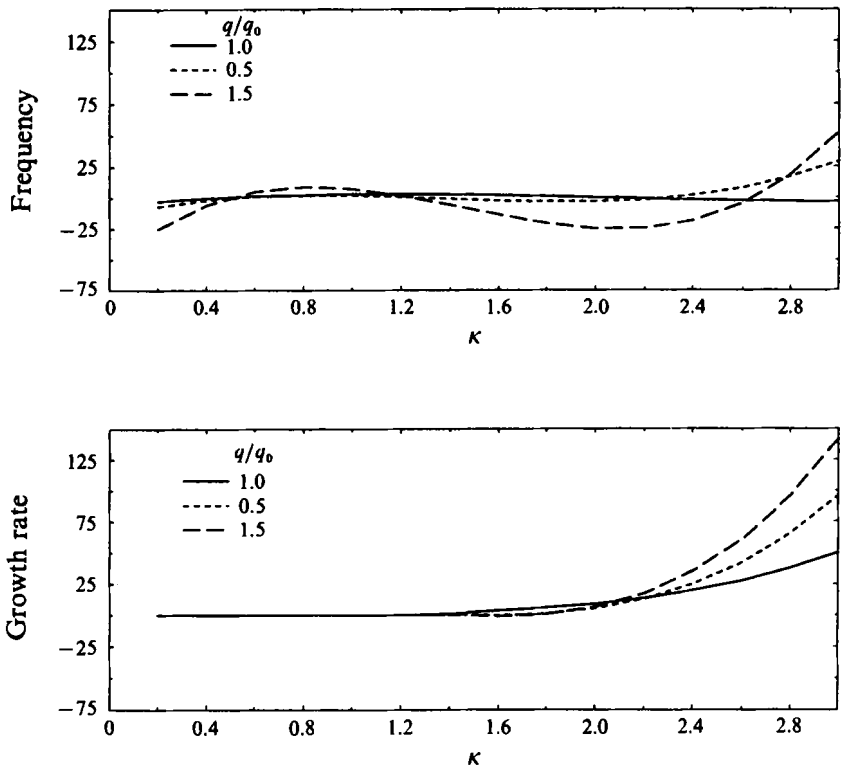

FIGURE 12. Growth rate and frequency as a function of κ at experimental aspect ratio = 4.54 for various q/q_0 values for corotating disks for azimuthal wavenumber $n = 2$.

4.2. *Finite container geometry*

For $\alpha > 0$, the radial dependence of the base state (33)–(35) suggests a Galerkin basis

$$R_\lambda \equiv R_l(r) = \frac{\sqrt{2}J_1(\lambda r)}{J_0(\lambda)}, \quad \lambda = \lambda_l, \quad l = 1, 2, \ldots, \tag{74}$$

where λ_l are roots of the Bessel functions $J_1(\lambda)$. As is well known, the $R_l(r)$ form a complete orthonormal set on (0, 1), with

$$\int_0^1 r R_k(r)\, R_l(r)\, \mathrm{d}r = \delta_{kl}. \tag{75}$$

with this choice of $R_l(r)$ and $Z_m(z)$, we follow the same method of solution as described before, with eigenvalue problem of the form (53).

4.2.1. *Results and discussion*

Figures 11 (*a*) and 11 (*b*) present relief plots of the computed growth rates $\mathrm{Re}(\sigma)$, and frequencies $\mathrm{Im}(\sigma)$ as a function of α^{-1} and κ for corotating disks, with q taken equal to q_0. The same plots for counter-rotating disks exhibit qualitatively similar behaviour. From figure 11 (*a*), one sees that the flow is always unstable for $\kappa > 0$. However, the growth rate is quite small (< 0.001) until κ attains a certain critical range of values. This behaviour is observed over a range of aspect ratios including those representative of our experimental set-up.

Figure 12, obtained by taking slices through figure 11 (*a*), shows the growth rate and frequency as a function of κ for an aspect ratio that corresponds approximately to our

	κ		
α	-0.1	0	0.1
10^{-6}	-1.3×10^{3}	0	1.29×10^{5}
10^{-5}	-1.2×10^{2}	0	1.32×10^{5}
10^{-4}	-2.1×10^{-2}	0	2.29×10^{-5}
10^{-3}	-1.1×10^{-3}	0	1.7×10^{-5}
10^{-2}	-1.4×10^{-2}	0	1.6×10^{-7}
10^{-1}	-1.8×10^{-2}	0	2.3×10^{-8}

TABLE 2. Growth rate as function of (α, κ)

experiment, at various q. One sees that the results are not sensitive to q. We should note that the actual experimental apparatus differs from the idealized finite container geometry (figure 5) by the presence of solid retainer rings of width ≈ 1.5 cm at the edge of the porous disks (figure 1). We have chosen the sidewall radius to define the aspect ratio in figure 12 for purposes of comparison with experiment. The experimental value of a critical $\kappa \approx 2.0$ obviously differs somewhat from the value of $\kappa \approx 1.6$ which one might infer from figure 12.

From our computations, we find that for large aspect ratios the growth rate increases rapidly, attaining large values even for small κ, as in the case of similarity flow. Furthermore, the instability is always oscillatory in nature. We find a growth rate almost independent of, and a frequency linearly dependent on, the azimuthal wavenumber. The almost complete independence of growth rate from n is indicative of 'form-preserving' instability with no preferred azimuthal mode.

The curious dependence of growth rate on κ discussed above represents an unusual type of bifurcation at $\kappa = 0$. This is revealed more clearly by recognizing that the negative real axis $\kappa < 0$ corresponds to suction instead of injection at the disk which, although inaccessible to us in our current experimental set-up, arises mathematically from a reversal of signs on W_0 in (11), and, hence, on q and ψ in (22)–(35). The calculation of §4.2 carries through, *mutatis mutandi*, and table 2 give select values of computed growth rates as a function of κ and α. As seen from the table, the flow appears very strongly stable for $\kappa < 0$ and $\alpha > 0$ but, in accord with the previous calculations, exhibits extremely large growth rates for $\kappa > 0$ as $\alpha \to 0$, such as to suggest a pitchfork bifurcation at $\kappa = 0$ for $\alpha = 0$.

Of course, one should not expect the local behaviour near $\kappa = 0$ to persist for all $\kappa < 0$, given the complex bifurcations of suction-type flows revealed in the work of Goldshtik & Javorsky (1989). As a further qualification, we note that a stability calculation based on the representation (63) for the similarity limit $\alpha \to 0$ gave large positive growth rates even for $\kappa = 0$. From this, we are led to conclude tentatively that the singularity of (66) for $r \to \infty$ with $\mathrm{Re}(\lambda) > 0$ renders it wholly unsuitable for the suction-type flow, essentially because unbounded disturbances in the far field are swept radially inward by the base flow.

In view of the numerically predicted growth rates for $\kappa > 0$, the apparent stability for $0 < \kappa \leqslant 2.0$ observed in our experiments still calls for theoretical explanation, and several possibilities come to mind. While it is conceivable that our linear stability analysis may fail to capture certain convective stabilization effects for $\alpha > 0$, it seems more plausible to us that finite-amplitude nonlinear effects may be implicated. To facilitate further discussion of such effects, it is worthwhile recalling a degenerate, 'transcritical' version of the canonical algebraic form for the unfolding of a pitchfork

bifurcation, as cited e.g. by Drazin & Reid (1989, p. 414 ff.) or Golubitsky & Schaeffer (1985, Section 4, p. 207, Case No. 6):

$$x^3 - \sigma x + \delta x^2 = 0. \tag{76}$$

Here x represents disturbance amplitude and $\sigma = \sigma(\kappa, \alpha)$ growth rate, while $\delta = \delta(\alpha)$ is a parameter such that $\delta(\alpha) \to 0$ for $\alpha \to 0$. The most direct interpretation of our experiments is provided by the (Landau) scenario, $\delta \equiv 0$, with small amplitude x proportional to $\sigma^{\frac{1}{2}}$ and with $\sigma(\kappa, \alpha)$ given by our linear stability analysis. However, one cannot rule out a more subtle imperfect (transcritical) bifurcation arising for $\delta \neq 0$, with x lying on the low-amplitude branch, at least up to $\kappa \approx 2$, followed by a further bifurcation or transition to the larger amplitude branch for $\kappa \geqslant 2$. Such transition or bifurcation is plausible in view of the large growth rates for $\kappa \geqslant 2$ associated with the nearby base state.

In conclusion, the linear stability analysis presented above suggests that, in the absence of confinement, swirl always destabilizes the axisymmetric stagnation-point flow in the high-*Re* regime, while sidewall confinement has a strongly stabilizing influence which results in a phenomenon with many features of an imperfect bifurcation. As viscosity is found to stabilize the unconfined similarity flow, it might be possible to stabilize the base flow over a wide range of Rossby numbers *Ro*, possibly into the rotation-dominated injection regime $Ro \leqslant \pi^{-1}$, by the combined effects of viscosity and sidewall confinement, as may already be suggested by the experiments of Chen *et al.* (1987). This appears worthy of further theoretical and experimental study, which we are currently pursuing.

While the mass transfer technique developed here provides a convenient measurement of transport characteristics of the base flow and a rather sensitive indicator of instability, it is at best a qualitative tool. This is reflected by the large departures from the baseline shown in figures 2 and 3, which must arise from convection effects that could not be explained by linear disturbances on near-similarity flows. Hence, part of our ongoing experimental work is aimed at direct observation of flow velocities.

This work was supported in part by National Science Foundation Grants CTS-9023696 and CTS-9196226. Also, acknowledgement is made to the Donors of the Petroleum Research Fund, administered by the American Chemical Society, for partial support of the research, through Grant ACS/PRF 23120-AC7-C. We should further like to thank Mr Jin Yang, Mr Yifan Zhu and various other personnel at the University of Southern California for their efforts in the early stages of the experimental work reported above.

Appendix. First-order (outer) viscous corrections

The corrected form of the results given by Zhang & Goddard (1989) is

$$\begin{aligned} H_1 = &-\frac{(2\beta+1)\kappa}{2\beta(1+\beta)} \sin 2x \ln|\beta + \cos^2 x| - \frac{\kappa \sin 2x}{\beta(1+\beta)} \int_0^x M(x)\,\mathrm{d}x \\ &+ \left[\frac{2\beta}{1+\beta}\sin^2 x - \frac{2(1+\beta)}{\beta}\cos^2 x\right] \kappa M(x) \\ &+ \kappa[x \sin 2x + 2(1+\beta)^2 \cos 2x] I_1 + I_2 \kappa \sin 2x, \end{aligned} \tag{A 1}$$

$$G_1 = \kappa H_1 - \frac{2\beta+1}{2\beta(\beta+1)}\sin 2x - (\beta+\cos^2 x)\left[I_1 - \frac{M(x)}{\beta(\beta+1)}\right], \tag{A 2}$$

where $\beta = -\dfrac{1+\cos\kappa}{2}$, $x = \kappa[z - \operatorname{sgn}(\frac{1}{2}z)]$, $M(x) = \displaystyle\int_0^x \frac{\mathrm{d}x}{\beta+\cos^2 x}$

$$I_1 = \int_{-\kappa/2}^{0} \frac{\mathrm{d}x}{\beta+\cos^2 x}, \quad I_2 = \frac{2\ln|\beta|-1}{\beta} - 2\int_{-\kappa/2}^{0} M(x)\,\mathrm{d}x \frac{1}{\beta(1+\beta)}.$$

REFERENCES

ACRIVOS, A. & GODDARD, J. D. 1966 Asymptotic expansions for laminar forced-convection heat and mass transfer, Part 1. Boundary layer flows. *J. Fluid Mech.* **24**, 339.

BATCHELOR, G. K. 1951 Note on a class of solutions of the Navier–Stokes equations representing steady rotationally-symmetric flow. *Q. J. Mech. Appl. Maths* **4**, 29.

BATCHELOR, G. K. 1967 *An Introduction to Fluid Dynamics*. Cambridge University Press.

BODONYI, R. J. & NG, B. S. 1983 On the stability of the similarity solutions for swirling flow above an infinite rotating disk. *J. Fluid Mech.* **144**, 311.

BRADY, J. F. & DURLOFSKY, L. 1987 On rotating disk flow. *J. Fluid Mech.* **175**, 363.

BRATTKUS, K. & DAVIS, S. H. 1990 The linear stability of plane stagnation-point flow against general disturbances. *Q. J. Mech. Appl. Maths* **43**, 471.

CHEN, K. K. & LIBBY, P. A. 1968 Boundary layers with small departures from Falkner–Skan profile. *J. Fluid Mech.* **33**, 273.

CHEN, Z. H., LIU, G. E. & SOHRAB, S. H. 1987 Premixed flames in counterflowing jets under rigid-body rotation. *Combust. Sci. Tech.* **51**, 39.

DRAZIN, P. G. & REID, W. H. 1989 *Hydrodynamic Stability*. Cambridge University Press.

ERDÉLYI, A. (ED.) 1954 *Tables of Integral Transforms*. McGraw-Hill.

FALLER, A. J. 1991 Instability and transition of disturbed flow over a rotating disk. *J. Fluid Mech.* **230**, 245.

FLETCHER, A. J. 1984 *Computational Galerkin Method*. Springer.

FRAENKEL, L. E. 1953 On the flow of rotating fluid past bodies in a pipe. *Proc. R. Soc.* A **233**, 506.

GODDARD, J. D., MELVILLE, J. B. & ZHANG, K. 1987 Similarity solution for stratified rotating-disk flow. *J. Fluid Mech.* **182**, 427.

GOLDSHTIK, M. A. & JAVORSKY, N. J. 1989 On the flow between a porous rotating disk and a plane. *J. Fluid Mech.* **207**, 1.

GOLUBITSKY, M. & SCHAEFFER, D. G. 1985 *Singularities and Groups in Bifurcation Theory*. Springer.

GORDON, L. S., NEWMAN, J. S. & TOBIAS, C. W. 1966 The role of ionic migration in electrolytic mass transport; diffusivities of $[Fe(CN)_6]^{3-}$ and $[Fe(CN)_6]^{4-}$ in KOH and NaOH solutions. *Ber. Bunsengellschaft* **4**, 414–420.

GREENSPAN, H. P. 1968 *The Theory of Rotating Fluids*. Cambridge University Press.

GREGORY, N., STUART, J. T. & WALKER, W. S. 1955 On the stability of three-dimensional boundary layers with application to a rotating disk. *Phil. Trans. R. Soc. Lond.* A **248**, 155.

KIM, J. S., LIBBY, P. A. & WILLIAMS, F. A. 1992 Influence of swirl on the structure and extinction of strained premixed flames. *Phys. Fluids* A **4**, 391.

MALIK, M. R. 1986 The neutral curve for stationary disturbance in rotating-disk flow. *J. Fluid Mech.* **164**, 275.

PARTER, S. V. & RAJAGOPAL, K. R. 1984 Swirling flow between rotating plates. *Arch. Rat. Mech. Anal.* **86**, 305.

SIVASHINSKY, G. I. & SOHRAB, S. H. 1987 The influence of rotation on premixed flames in stagnation point flow. *Combust. Sci. Tech.* **53**, 67.

SZERI, A. Z., GIRON, A. & SCHNEIDER, S. J. 1983 Flow between rotating disks. Part 2. Stability. *J. Fluid Mech.* **134**, 133.

WU, C.-Y. 1991 An electrochemical study of mass transfer between rotating counterflowing fluid streams. M.S. thesis, University of Southern California.

YIH, C.-S. 1980 *Stratified Flows.* Academic.

ZANDBERGEN, P. J. & DIJKSTRA, D. 1987 Von Kármán swirling flows. *Ann. Rev. Fluid Mech.* **19**, 465.

ZHANG, K. & GODDARD, J. D. 1989 Viscous interlayer structure and transport properties in von Kármán swirling flows. *Phys. Fluids* A **1**, 132.